JOURNAL OF GEOPHYSICAL RESEARCH, VOL. 113, D21117, doi:10.1029/2008JD010607, 2008

Integration of a prognostic sea surface skin temperature scheme into weather and climate models

Michael A. Brunke,[1] Xubin Zeng,[1] Vasubandhu Misra,[2] and Anton Beljaars[3]

Received 13 June 2008; revised 20 August 2008; accepted 27 August 2008; published 12 November 2008.

[1] A prognostic skin sea surface temperature (SST) algorithm is included in the Community Atmosphere Model (CAM3.1). With this algorithm, the model produces a mean diurnal cycle of <0.5 K over most oceanic regions and >0.5 K primarily in tropical and subtropical oceans of the summer hemisphere with isolated areas of >2 K. The diurnal cycle in air temperature is substantially increased over regions with large skin SST diurnal cycles, and the enhanced diurnal cycle agrees better with the TAO buoy data over the equatorial Pacific. There is also a significant effect on the diurnal cycle in precipitation particularly in the increased hourly maximum precipitation over the Bay of Bengal and the western Pacific in boreal summer. These changes to the diurnal cycle in SST affect the seasonal climatologies in the model with improved seasonal mean precipitation mainly in the tropics following similar patterns to the hourly maximum precipitation rates. The near-surface flow across the Indian subcontinent is also increased during the summer monsoon resulting in higher seasonal precipitation over the Bay of Bengal.

Citation: Brunke, M. A., X. Zeng, V. Misra, and A. Beljaars (2008), Integration of a prognostic sea surface skin temperature scheme into weather and climate models, *J. Geophys. Res.*, *113*, D21117, doi:10.1029/2008JD010607.

1. Introduction

[2] Numerical weather prediction (NWP) models and atmospheric general circulation models (AGCMs) both utilize bulk turbulent flux algorithms to calculate sensible and latent heat fluxes as the lower boundary condition of the model. One of the fundamental values needed by these bulk algorithms is sea surface temperature (SST). Fundamentally, this value should be literally the temperature at the atmosphere-ocean interface. However if an AGCM is coupled to an oceanic general circulation model (OGCM), this value is taken as the average temperature in the uppermost layer of the OGCM with a typical depth of 10 m. NWP models and uncoupled AGCMs utilize a pentad- to monthly averaged SST product such as *Reynolds and Smith* [1994] which is a blend of satellite retrievals and in-situ measurements from ships and buoys at depths ranging from several cm to a few m.

[3] The difference between the latter temperature, referred to as bulk temperature (T_b), and the actual interfacial temperature or skin temperature (T_s) comes about because of two processes. Within the first few mm, there is a net cooling in the molecular sublayer, producing a cool skin. Additionally during the day, a warm layer is established because of the absorption of incoming shortwave radiation. The temperature difference across this warm layer can be as large as 3 K [*Fairall et al.*, 1996]. Thus

$$T_s = T_b - \Delta T_c + \Delta T_w \tag{1}$$

where ΔT_c and ΔT_w are the temperature differences across the cool skin and warm layer respectively [*Fairall et al.*, 1996]. According to *Fairall et al.* [1996], the net surface heat fluxes computed using T_s instead of T_b differ by 11 W m^{-2} averaged over the Tropical Ocean-Global Atmosphere Coupled Ocean-Atmosphere Response Experiment (TOGA COARE) period but could be as high as $\sim$50 W m^{-2} at any particular hour though. Thus the difference between T_b and T_s should be accounted for in the model. Recently, several groups [e.g., *Fairall et al.*, 1996; *Clayson and Curry*, 1996; *Gentemann et al.*, 2003; *Zeng et al.*, 1999] have developed schemes to determine T_s. Most of these, however, are unsuitable for modeling purposes, because they are not rigorous enough, utilize a fixed diurnal cycle in T_s, or need the diurnal cycle of bulk temperature as input. On the other hand, *Beljaars* [1997] developed a prognostic scheme on the basis of the diagnostic relationships developed by *Webster et al.* [1996].

[4] An alternative is the recently developed prognostic scheme of *Zeng and Beljaars* [2005] (hereafter referred to as ZB). This scheme implements rigorously derived equations for the cool skin and warm layer effects. It produced realistic diurnal cycles when using observed surface fluxes in both tropical and mid-latitude locations. When preliminarily implemented into a three-member ensemble of the ECMWF model, it produced changes to the annual average latent heat flux in excess of 10 W m^{-2} in some oceanic regions.

---

[1] Institute of Atmospheric Physics, University of Arizona, Tucson, Arizona, USA.

[2] Department of Meteorology, Florida State University, Tallahassee, Florida, USA.

[3] European Centre for Medium-Range Weather Forecasts, Reading, UK.

0148-0227/08/2008JD010607$09.00

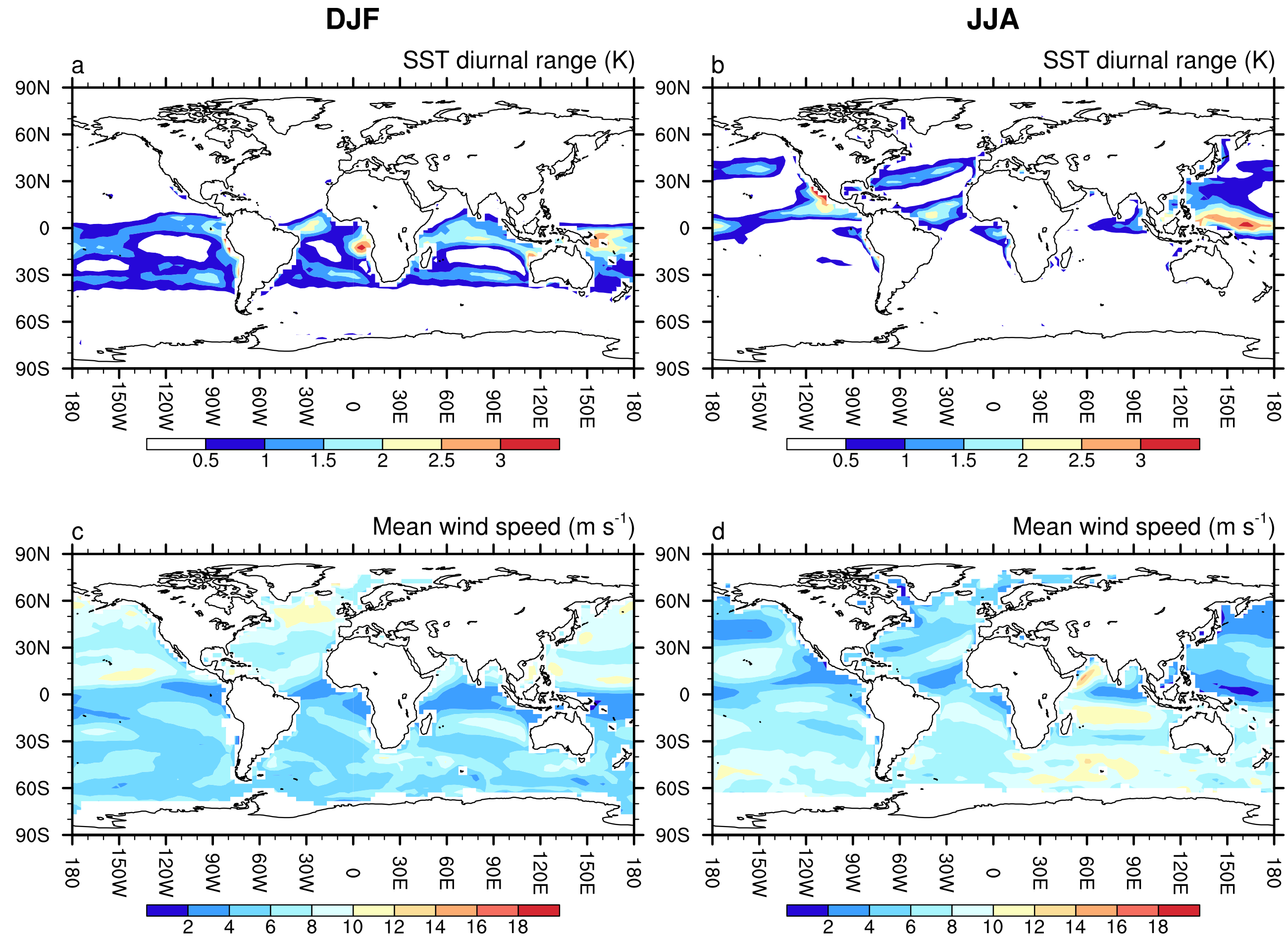

Figure 1. (a, b) The mean diurnal range, i.e., the difference between the daily maximum and minimum, in sea surface temperature (SST) in TSKIN for December–February (DJF) of year 4/5 and for June–August (JJA) of year 5 respectively. (c, d) The mean 10-m wind speed in TSKIN for DJF of year 4/5 and for JJA of year 5 respectively.

[5] In this study, ZB is implemented into an AGCM, the National Center for Atmospheric Research (NCAR) Community Atmosphere Model version 3.1 (CAM3.1). The impact of the skin SST on the simulated climate from this model is discussed here. The model is described in section 2, and the validation data used in this study is described in section 3. The model results are compared with the validation data in section 4. Finally, these results are summarized, discussed, and compared to two other climate and numerical weather prediction models in section 5.

2. Model Description

[6] CAM3.1 is the latest version of NCAR's AGCM released to the community. It can be run using a choice of three dynamical cores: a spectral Eulerian, a semi-Lagrangian, and a finite volume. CAM3.1 can be implemented into the Community Climate System Model in which it is fully coupled with the Community Land Model (CLM); the Community Sea Ice Model (CSIM); and an ocean model, the Parallel Ocean Program (POP) model. It can also be run as a stand-alone model coupled only to the CLM [*Collins et al.*, 2006b]. This latter configuration is comparable to the historical Community Climate Model (CCM) which is considered to be a preceding version of CAM3.1. When in stand-alone mode, CAM3.1 utilizes a thermodynamic sea ice formulation on the basis of the physics in the CSIM and either a slab ocean model or an SST product. When the SST product is used, the sea ice formulation simply calculates surface fluxes on the basis of climatological sea ice extent [*Collins et al.*, 2006a]. The SST product is a blend of the Hadley Centre Sea Ice and Sea Surface Temperature (HadISST) data set [*Rayner et al.*, 2003] prior to 1981 and the *Reynolds et al.* [2002] data set after 1981. More details on the configuration of this model can be found in *Collins et al.* [2004, 2006a].

[7] In this study, CAM3.1 has been run in stand-alone mode with the Eulerian dynamical core with a spectral truncation of T42 corresponding roughly to a horizontal resolution of 2.8°. A climatological annual cycle of SST is used so that every year has the same annual cycle of SST. There are three versions of CAM3.1 presented here: the unaltered version (CONTROL), a version utilizing ZB (TSKIN) in which the skin temperature correction is added to the climatological SST, and a version adding a random perturbation uniformly distributed between +0.1 and −0.1 K

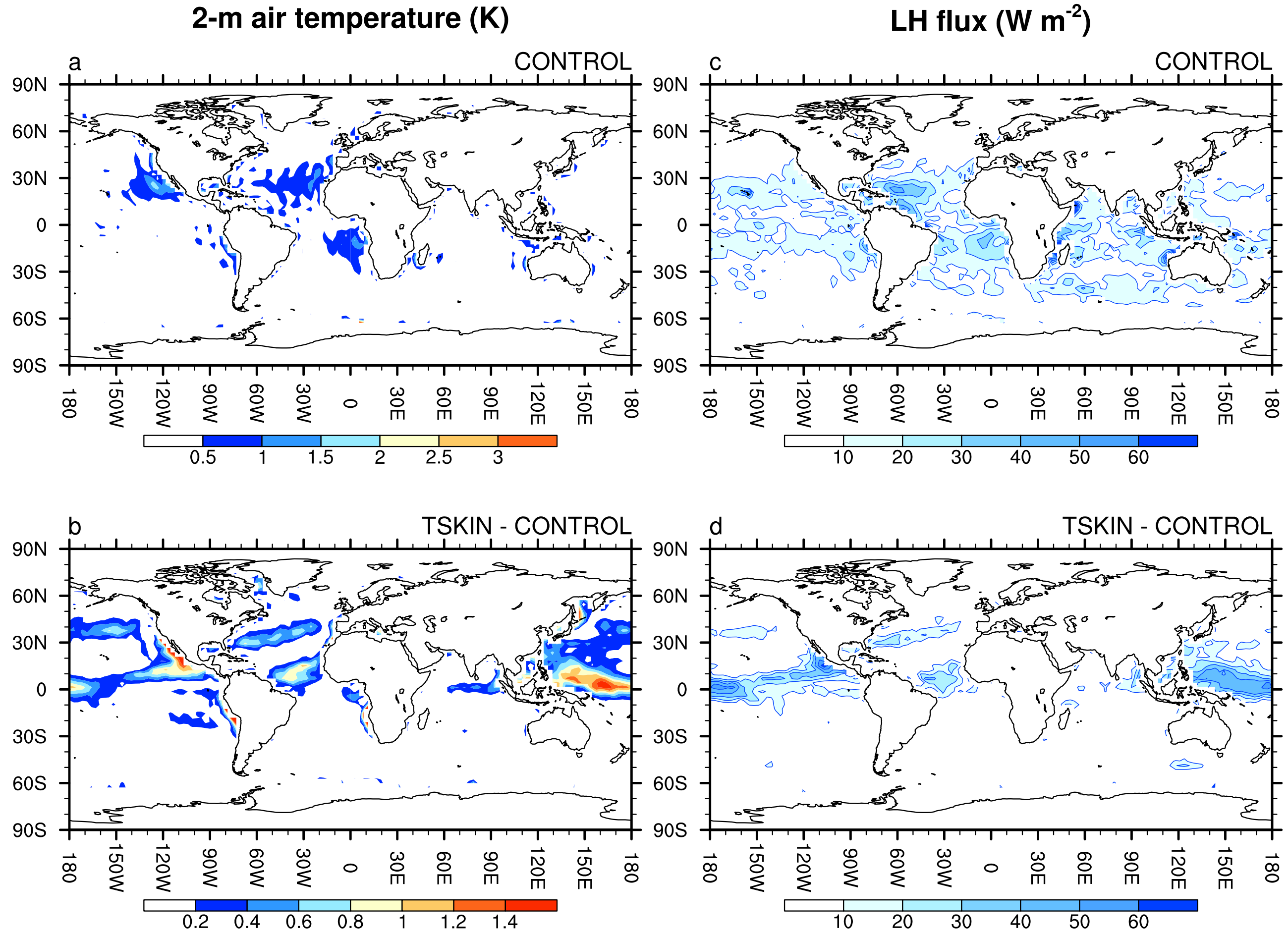

Figure 2. (a) The mean diurnal range in the 2-m air temperature in JJA of year 5 for CONTROL and (b) the mean difference in diurnal range between that of TSKIN and CONTROL. (c) The mean diurnal range in the surface latent heat flux in JJA of year 5 for CONTROL and (d) the mean difference in diurnal range between that of TSKIN and CONTROL.

to the climatological SST (RANDOM). Thus the skin SST effect can be demonstrated only when the differences between CONTROL and TSKIN are statistically significant and also larger in magnitude than those between CONTROL and RANDOM. Each of these model versions are run for 20 years outputting monthly average values, and hourly output is produced for one boreal winter and summer season (see section 4.1).

3. Data

[8] Most of the validation data used in this study are from the latest ECMWF Reanalysis (ERA-40) [*Uppala et al.*, 2005] obtained online from the ECMWF data server (http://data.ecmwf.int/data/). ERA-40 includes improvements from the previous ERA-15 such as a three-dimensional variational data assimilation system; 60 model layers (compared to 31 in ERA-15); improved model parameterizations for deep convection, radiation, clouds, orography, the stable boundary layer, and land surface; and a new representation of sea ice. ERA-40 data are available for 45 years from September 1957 to August 2002 [*Uppala et al.*, 2005] for 23 pressure levels at a horizontal resolution of 2.5°. Here, comparisons are made with 20 years of data from January 1981 to December 2000.

[9] Gridded precipitation data are taken from the Climate Prediction Center Merged Analysis of Precipitation (CMAP) [*Xie and Arkin*, 1997] obtained online from the National Oceanic and Atmospheric Administration (NOAA) Earth System Research Laboratory (ESRL) data server (http://www.cdc.noaa.gov/). This 27-year data set is derived by merging surface rain gauge data with satellite estimates. The data are available at monthly and pentad time scales at a horizontal resolution of 2.5°. Here, only 20 years are used from January 1981 to December 2000.

[10] The model hourly precipitation is also compared to that of the Tropical Rain Measuring Mission (TRMM) 3B42 product. This product is composed of 3-hourly derived precipitation rates for 1998 to the present at a horizontal resolution of 0.5°. The rates are derived from geosynchronous satellite measurements using an algorithm that has been tuned using measurements made by the TRMM Microwave Imager (TMI) and Visible Infrared Scanner (VIRS) [*Rasch et al.*, 2006]. The actual TMI and VIRS measurements are of limited utility here to investigate short-

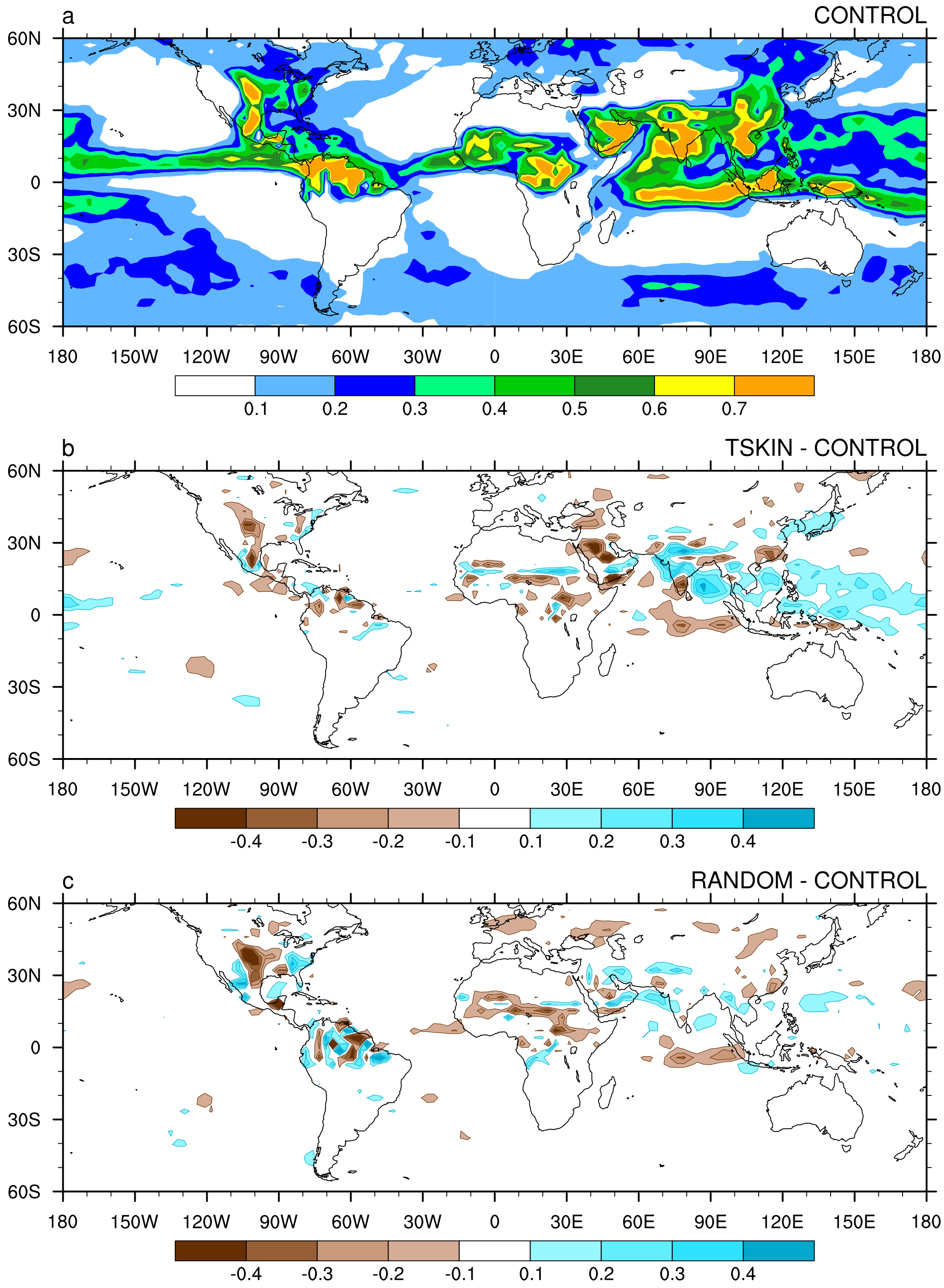

Figure 3. (a) The maximum precipitation rate (mm hr^{-1}) in the mean diurnal cycle in JJA of year 5 for CONTROL and (b) the difference between the maximum in TSKIN versus CONTROL and (c) in RANDOM versus CONTROL.

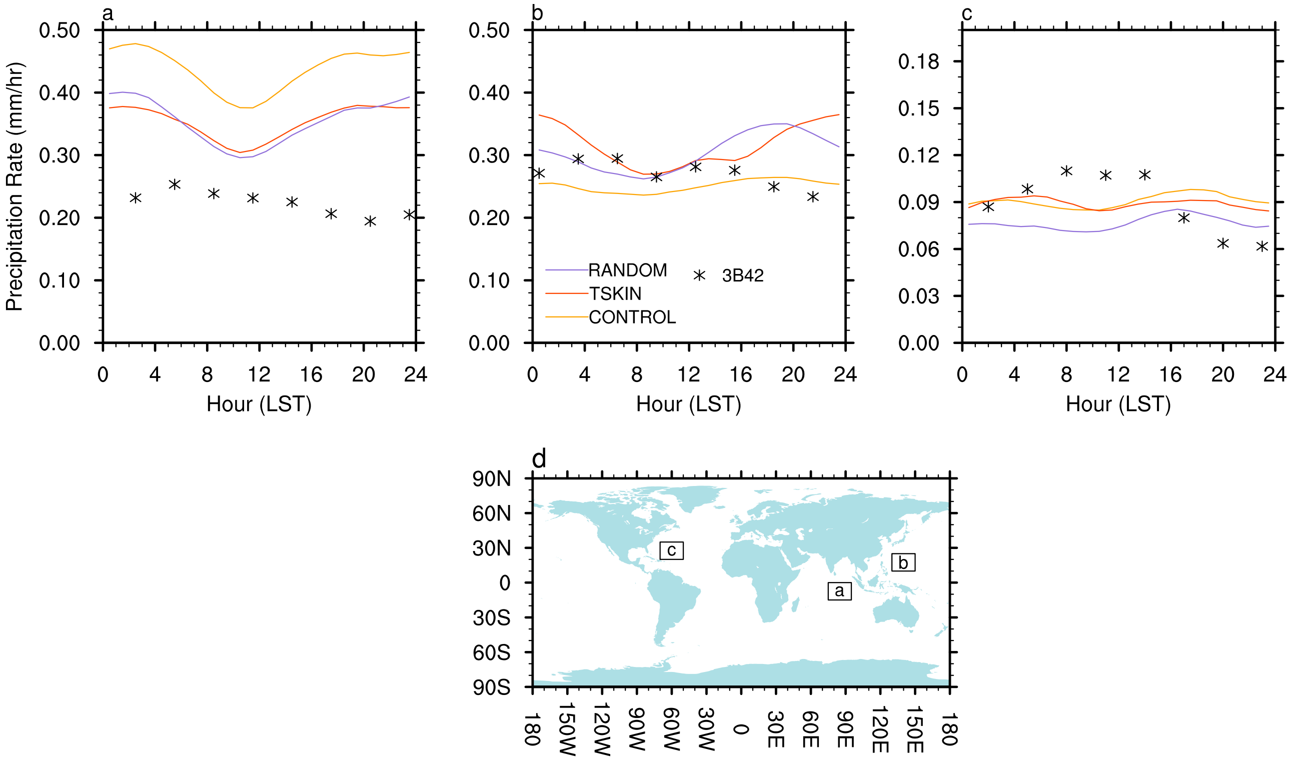

Figure 4. The mean hourly precipitation rates for JJA of year 5 in CONTROL, TSKIN, and RANDOM and for 1988–2006 in the TRMM 3B42 product for (a) 75–95°E, 0–15°S over the Indian Ocean, (b) 130–150°E, 10–25°N over the northwest Pacific Ocean, and (c) 50–70°W, 20–35°N over the northwest Atlantic Ocean. These three regions are displayed on the map in Figure 4d for convenience. Note the difference in the *y* axes in Figures 4a and 4b versus 4c.

time-scale phenomena unless a compositing technique is used [e.g., *Negri et al.*, 2002] because of its limited temporal sampling frequency.

[11] The model results are compared to measurements made by the buoys in the Tropical Atmosphere-Ocean/Triangle Trans-Ocean Buoy Network (TAO/TRITON, hereafter referred to simply as TAO) in the tropical Pacific from 137°E to 95°W between roughly 10°N and 10°S [*McPhaden et al.*, 1998]. TAO uses Autonomous Temperature Line Acquisition System (ATLAS) buoys to measure air temperature and relative humidity at a height of 3 m as well as wind speed and direction at a height of 4 m. Some of the newer ATLAS buoys also measure incoming solar radiation and precipitation [*Serra et al.*, 2001]. Here, we compare the model results with all of these measurements where available in the buoy array.

[12] The model intraseasonal oscillations are finally compared to those observed in outgoing longwave radiation (OLR) as measured by NOAA's polar-orbiting satellites [*Gruber and Krueger*, 1984; *Liebmann and Smith*, 1996] obtained from the NOAA ESRL data server (http://www.cdc.noaa.gov/). These have been used extensively as a proxy for precipitation, as it distinguishes areas of deep convection [e.g., *Arkin and Ardanuy*, 1989]. Similar to *Wheeler and Kiladis* [1999], the OLR data from January 1981 to December 2000 are divided into 96-day overlapping segments and into its symmetric and antisymmetric components. Then, double FFTs are performed on these components to get their spectra and compared to similarly prepared spectra from CONTROL and TSKIN.

4. Results

4.1. Diurnal Cycle

[13] First, we examine the diurnal cycles in SST produced in TSKIN during one boreal winter season (December–February or DJF) in years 4 and 5 and one boreal summer season (June–August or JJA) of year 5. This is done by looking at the diurnal range, i.e., the difference between the maximum and minimum hourly values, in the mean seasonal diurnal cycle as shown in Figures 1a and 1b. In both DJF and JJA, the SST diurnal ranges are <0.5 K in most oceanic regions but >0.5 K principally in the tropical and subtropical oceans of the summer hemisphere with isolated areas (e.g., the western Pacific warm pool in JJA) of >2 K. Comparison to the mean near-surface wind speed (Figures 1c and 1d) shows that the areas of highest SST diurnal range occur in areas of light wind speeds (<~4 m s^{-1}) as would be expected.

[14] The increased diurnal cycle in SST in some areas of the world has an effect on the near-surface air temperature over those regions. Even though there is no diurnal variation of SST in CONTROL, there is still a small (generally <0.5 K over most oceanic regions) diurnal cycle in 2-m air temperature as shown in Figure 2a in JJA because of the diurnal cycle of radiation. A diurnal range over

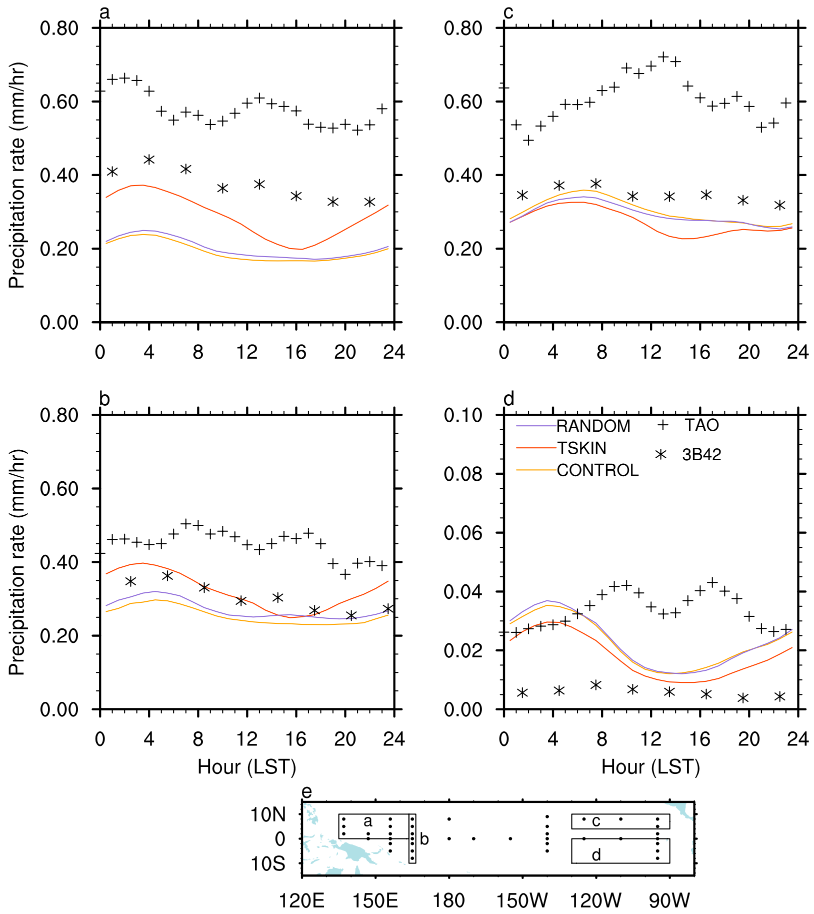

Figure 5. The mean hourly precipitation rates in JJA from CONTROL, TSKIN, and RANDOM as well as from the TAO buoys and the mean 3-hourly precipitation rates from the TRMM 3B42 product (a) in the region of the northwest Pacific bounded by 130–163.6°E and 0–10°N, (b) along the 165°E longitude line, (c) in the northeast Pacific ITCZ from 130°–90°W and 4°–10°N, and (d) in the southeast Pacific from 130°–90°W and 0°–10°S. These regions are displayed on the map in Figure 5e for convenience along with the TAO buoys that are included in each. Note the difference in the *y* axes in Figures 5a–5c versus 5d.

oceans of ~0°–0.4°C also appeared in the fully coupled CCSM which was shown to be too small compared to the NCEP/NCAR reanalysis [*Dai and Trenberth*, 2004]. This was attributed to the lack of a diurnal cycle in SST. In TSKIN, the mean diurnal range in hourly 2-m air temperature is substantially increased in roughly the same areas where there is increased SST diurnal range. For example, the diurnal range over some parts of the western equatorial Pacific is about three times higher in TSKIN (Figure 2b) compared to CONTROL (Figure 2a). On the other hand, the 2-m air temperature diurnal range in RANDOM is essentially the same as that in CONTROL over most oceanic regions (not shown). Similar results are obtained in DJF with the subtropical regions of highest diurnal range mainly in the Southern Hemisphere (not shown).

[15] The increased SST diurnal cycle in TSKIN also affects the diurnal cycle in surface fluxes, particularly the surface turbulent fluxes of latent and sensible heat. Figure 2d shows that in JJA the diurnal range in hourly latent heat flux is substantially increased in roughly the same areas where the diurnal range in SST is increased in TSKIN relative to CONTROL. Again, RANDOM's diurnal ranges are essentially the same as in CONTROL (not shown). The results for DJF are also similar with the highest diurnal range in the subtropical areas of the Southern Hemisphere (not shown).

[16] The diurnal range in hourly sensible heat flux is much smaller than that of the latent heat flux (not shown), because the mean sensible heat flux itself is much smaller. Even so, its diurnal range is substantially increased in TSKIN in areas where the SST diurnal range is also substantially higher relative to CONTROL.

[17] The SST diurnal cycle also impacts the diurnal cycle of precipitation, particularly over the tropical oceans. Figure 3a shows the maximum hourly precipitation rate in the mean JJA diurnal cycle in CONTROL. Also shown is the difference between TSKIN's maximum precipitation rate and that of CONTROL (Figure 3b). The largest increases in TSKIN are over the western Pacific between the equator and 30°N and over the Bay of Bengal, while differences are spatially incoherent over other oceanic regions. The differences between RANDOM and CONTROL are comparatively spatially incoherent over all

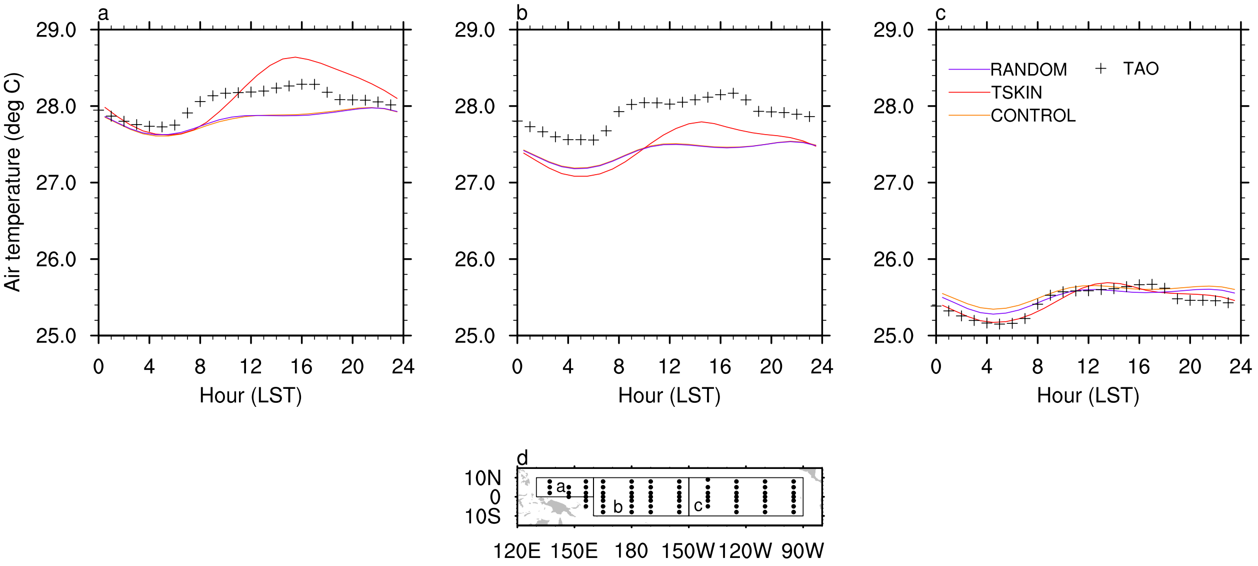

Figure 6. The mean hourly 3-m air temperature in JJA from CONTROL, TSKIN, and RANDOM with those of the TAO buoys (a) in a region of the northwest Pacific from 130°–170°E and 0°–10°N, (b) in the central Pacific from 170°E–150°W and 10°S–N, and (c) in the eastern Pacific from 150°–90°W and 10°S–N. The TAO buoys in each of these regions are shown on the map in Figure 6d for convenience.

oceanic regions (Figure 3c). In DJF, TSKIN produces similar results to JJA except reversed with an increased maximum precipitation rate along the southern side of the equator from 50°E to 150°W (not shown).

[18] To investigate the diurnal cycle of precipitation in these model experiments in greater detail, the mean hourly precipitation rates in JJA for several regions in the three model runs are compared to the mean three-hourly rates from the TRMM 3B42 product in Figure 4. In Region a over the Indian Ocean (75–95°E, 0–15°S, Figure 4a), CONTROL's precipitation rates are much higher than that of 3B42. These rates are reduced by similar amounts in both TSKIN and RANDOM, but they are still higher than 3B42. The maximum precipitation occurs in the early morning in all simulations which is a few hours earlier than in 3B42. The minimum precipitation occurs just before noon in all simulations in contrast to the early evening in 3B42.

[19] A radically different situation occurs in Region b over the northwest Pacific (130–150°E, 10–25°N, Figure 4b). Here, the precipitation rate is increased overall by both TSKIN and RANDOM, but the diurnal cycles between the two are quite different. RANDOM is very similar to CONTROL with a precipitation maximum erroneously in the early evening. TSKIN, however, produces a midnight maximum that is closer to the early morning maximum in 3B42 and even produces the midday secondary maximum that also appears in 3B42.

[20] A somewhat similar situation occurs in the northwest Atlantic (Region c; 50–70°W, 20–35°N, Figure 4c). CONTROL's maximum precipitation rate is in the early evening with a secondary maximum in the early morning. The rates in TSKIN are slightly increased in the early morning, while they are reduced slightly in the early evening. This, then, puts the maximum in TSKIN in the early morning a couple of hours before that in 3B42. In RANDOM, the precipitation rates are just reduced, and the maximum is simply pushed earlier by a couple of hours.

[21] The 3B42 product is limited in its temporal coverage, because it is only a three-hourly product. Thus the 3B42 precipitation rates and those from all three model runs are compared with those observed from the TAO buoy array in which some of the largest SST diurnal cycle changes are located. Figure 5 presents the mean precipitation in four regions: Region a in the western Pacific warm pool from 130–163.6°E and 0–10°N, Region b along the 165°E longitude line between 10°S–10°N, Region c in the intertropical convergence zone (ITCZ) of the northeast Pacific from 130°–90°W and 4–10°N, and Region d in the southeast Pacific from 130–90°W and 0–10°S. All model runs and 3B42 produce morning maximums in these four regions. CONTROL and RANDOM have similar hourly rates in all four regions, while TSKIN produces larger rates over the western Pacific (Regions a and b, Figures 5a and 5b) and lower rates over the southeastern Pacific (Region d, Figure 5d). In these regions, this makes TSKIN's results closer to 3B42 by on average 0.1, 0.03, and 0.005 mm hr^{-1} respectively.

[22] The hourly rates from the TAO buoys calculated as the average of six 10-min rates and smoothed using a 1-2-1 smoother are more variable despite the smoothing and much higher than 3B42 and most of the model results in all regions. Their diurnal cycles also differ from 3B42 and the models. In Region a (Figure 5a), there is an early morning maximum a couple of hours earlier than 3B42 and a lower secondary maximum coinciding with 3B42's. In Regions b (Figure 5b) and c (Figure 5c), the TAO buoys have maximum precipitation rates in the afternoon unlike 3B42. In Region d, the TAO buoys have maximum rates in the late morning and late afternoon. These results contrast with

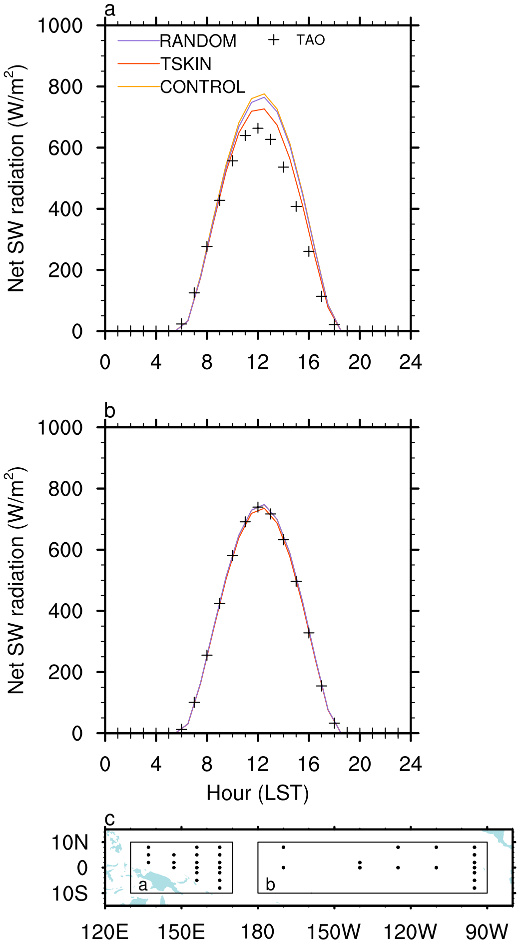

Figure 7. The mean 3-hourly net shortwave (SW) radiation in JJA from CONTROL, TSKIN, and RANDOM with those of the TAO buoys in (a) the eastern Pacific from 130°–170°E and 10°S–10°N and (b) the western Pacific from 180°–90°W and 10°S–10°N. These two regions are shown on the map in Figure 7c for convenience along with the TAO buoys that are included in each.

those of *Serra and McPhaden* [2004] who found morning precipitation maximums across the TAO array, but our average hourly rates, comparable to their conditional rates [*Serra and McPhaden*, 2003] or intensities [*Serra and McPhaden*, 2004] multiplied by precipitation frequency, were calculated to be consistent with the model results. Also, they were looking at six months (June to November), whereas we are looking at only three months (June to August). When the hourly average rates are averaged for June to November as in *Serra and McPhaden* [2004], the diurnal cycles are consistent with theirs in Regions b and c.

[23] This comparison illustrates the difficulty in defining precipitation amount. The 3B42 product and models are gridded averages, whereas the TAO values are point measurements. Also, the comparison with *Serra and McPhaden* [2004] demonstrates that how the rates are calculated also varies. Despite these complications, such a comparison is still useful, as it shows that the model timing of precipitation maxima and minima is largely unaffected by the use of the skin SST across the TAO array producing the early morning maximum as in 3B42. However, the skin SST diurnal cycle does produce precipitation rates closer to that of 3B42 in three of the four regions.

[24] Figure 6 compares the model diurnal cycles in air temperature which were adjusted to the 3-m measurement height of the TAO buoys. The diurnal cycle in the TAO buoys is very similar across the Pacific with an early morning minimum, a sharp increase for a few hours after sunrise, a more gradual increase to a maximum in the late afternoon, a sharp decrease for a few hours in the evening, followed by a gradual decrease toward the morning minimum. The diurnal cycles in CONTROL and RANDOM are essentially the same, correctly producing the early morning minimum but producing a primary maximum in the evening contrary to the buoy observations (with a primary maximum in the afternoon). The diurnal amplitude and mean temperatures for these simulations are also less than observed over Regions a (Figure 6a) and b (Figure 6b). TSKIN correctly produces an afternoon maximum and its mean diurnal range is also more realistic except in Region a (Figure 6a) where it is too high.

[25] Net shortwave radiation is also affected by the SST diurnal cycle in TSKIN. In Figure 7a TSKIN's mean net shortwave radiation in the western tropical Pacific is slightly lower during the midday maximum than that from CONTROL and RANDOM, more in line with that observed from the TAO buoys. Over the eastern tropical Pacific all model results agree with observations (Figure 7b).

4.2. Basic Climatology

[26] The overall effect of the SST diurnal cycle on the mean state of the model is investigated here by presenting the seasonal mean difference between TSKIN and CONTROL. With the implementation of ZB, the changes to the mean seasonal latent heat flux (TSKIN-CONTROL, Figure 8a) partially negate the errors in CONTROL over the tropics and some regions of the Southern Hemisphere as shown by the stippling. Some of these areas coincide with areas that have large diurnal skin SST ranges (Figure 1a). In areas with the slanted lines such as over the northwest Pacific and North Atlantic, the errors are accentuated further in TSKIN (Figure 8a). However, the interannual variation of this difference can be quite large, as much as >30 W m^{-2}, over some of these same regions (not shown). To quantify the effect of ZB versus some other model improvements, we also compute the differences between runs using observed SSTs between 1980 and 2000 of CAM3 and its earlier version (CAM2). The differences due to ZB are on the order of those between CAM3 and CAM2 with the average of $|\text{TSKIN} - \text{CONTROL}| - |\text{CAM3} - \text{CAM2}|$ being -2 W m^{-2}.

[27] In JJA (Figure 8b), there are larger differences (>30 W m^{-2}) than in DJF between the model runs in the vicinity of the South Asian monsoon region. The changes in latent heat flux in TSKIN actually lead to an improvement over the central Indian Ocean and the northwest and central tropical Pacific as indicated by the stippling. Again, some of these areas coincide with areas of large diurnal skin SST range in Figure 1b.

[28] A more significant improvement is made by the SST diurnal cycle in the mean precipitation rate, particularly in

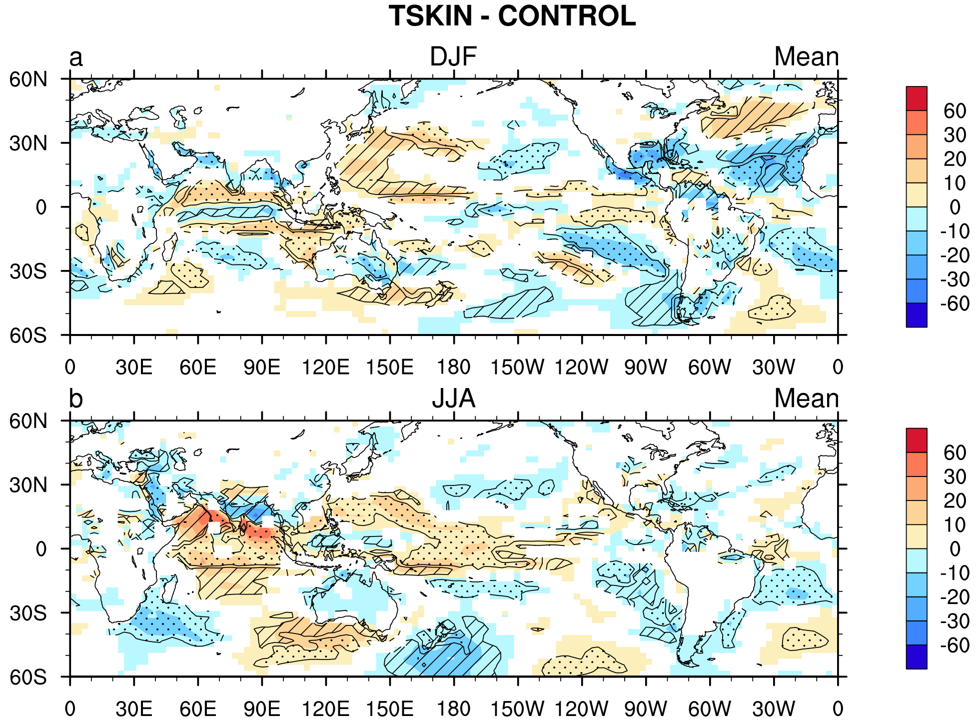

Figure 8. The 20-year mean difference in surface latent heat flux (W m^{-2}) between TSKIN and CONTROL in (a) DJF and (b) JJA for areas where this difference is 90% significant. Areas where the model is improved relative to ERA-40 ($|\mathrm{TSKIN} - \mathrm{ERA\text{-}40}| - |\mathrm{CONTROL} - \mathrm{ERA\text{-}40}| \leq -5$ W m^{-2}, stippled) and degraded ($|\mathrm{TSKIN} - \mathrm{ERA\text{-}40}| - |\mathrm{CONTROL} - \mathrm{ERA\text{-}40}| \geq 5$ W m^{-2}, slanted lines) are also indicated.

the tropics. Figure 9 shows the mean JJA precipitation rate (mm day^{-1}) in CONTROL (Figure 9a) as well as the mean difference between CONTROL and CMAP (Figure 9b), and that between CONTROL and TSKIN (Figure 9c). There is a statistically significant (at the 90% level) increase in TSKIN's precipitation rate in the northwest Pacific, the South China Sea, and the Bay of Bengal which alleviates the large underestimate in this quantity in CONTROL as indicated by the stippling (Figure 9c). There is also a statistically significant (at the 90% level) decrease in precipitation in the tropics along the south side of the equator over the Indian Ocean and the western Pacific Ocean as well as over the Arabian Sea and Peninsula in TSKIN which ameliorates some of the overestimate in these areas in CONTROL as indicated by the stippling (Figure 9c). Furthermore, some of the areas with the largest differences between model runs also have the largest interannual variability (>2 mm day^{-1}, Figure 9d). Again, these differences are also comparable to the difference between CAM3 and CAM2 with the average of $|\mathrm{TSKIN} - \mathrm{CONTROL}| - |\mathrm{CAM3} - \mathrm{CAM2}|$ being -0.2 mm day^{-1}.

[29] While TSKIN is able to alleviate some of the problems with tropical precipitation, it still is not able to fix some major deficiencies in the model. This can be seen in the seasonally averaged zonal precipitation between 60° and 180°E in which all model runs including CAM3 and CAM2 using observed SSTs incorrectly produce double ITCZs in JJA (Figure 10a) in contrast to the observed single ITCZ in both the CMAP and Global Precipitation Climatology Project (GPCP, also downloaded from the ESRL data server at http://www.cdc.noaa.gov) [*Adler et al.*, 2003] rates in the Northern Hemisphere and a single ITCZ in the Northern Hemisphere in DJF (Figure 10b) in contrast to the observed location in the Southern Hemisphere. A better situation occurs in the transitional seasons (boreal spring, March–May or MAM, Figure 10c, and boreal fall, September–November or SON, Figure 10d). CMAP and GPCP suggest that the precipitation should be higher in the fall hemisphere. While the model peak in the spring hemisphere ITCZ remains largely unchanged, the model precipitation generally falls between the CMAP and GPCP values in the rest of the tropics with TSKIN having the largest rates in the fall hemisphere ITCZ.

[30] The precipitation changes in the ITCZ and over the South Asian monsoon region in JJA are very similar to those of *Miller et al.* [1992] in ECMWF with an improvement to the parameterization of surface turbulent fluxes. They showed that their improved latent heat fluxes led to an enhancement of the large-scale flow. Particularly, there was an improved monsoon flow, which resulted in the improved monsoon precipitation as is seen here as well. In comparing Figure 11a (ERA-40) with Figure 11b (CONTROL), the model produces weaker cross-equatorial and cross-subcontinental flow than in ERA-40 which results in the model having lower wind speeds in the Bay of Bengal. As in *Miller et al.* [1992], these flows are strengthened in TSKIN (Figure 11c). The winds in the western Indian Ocean and

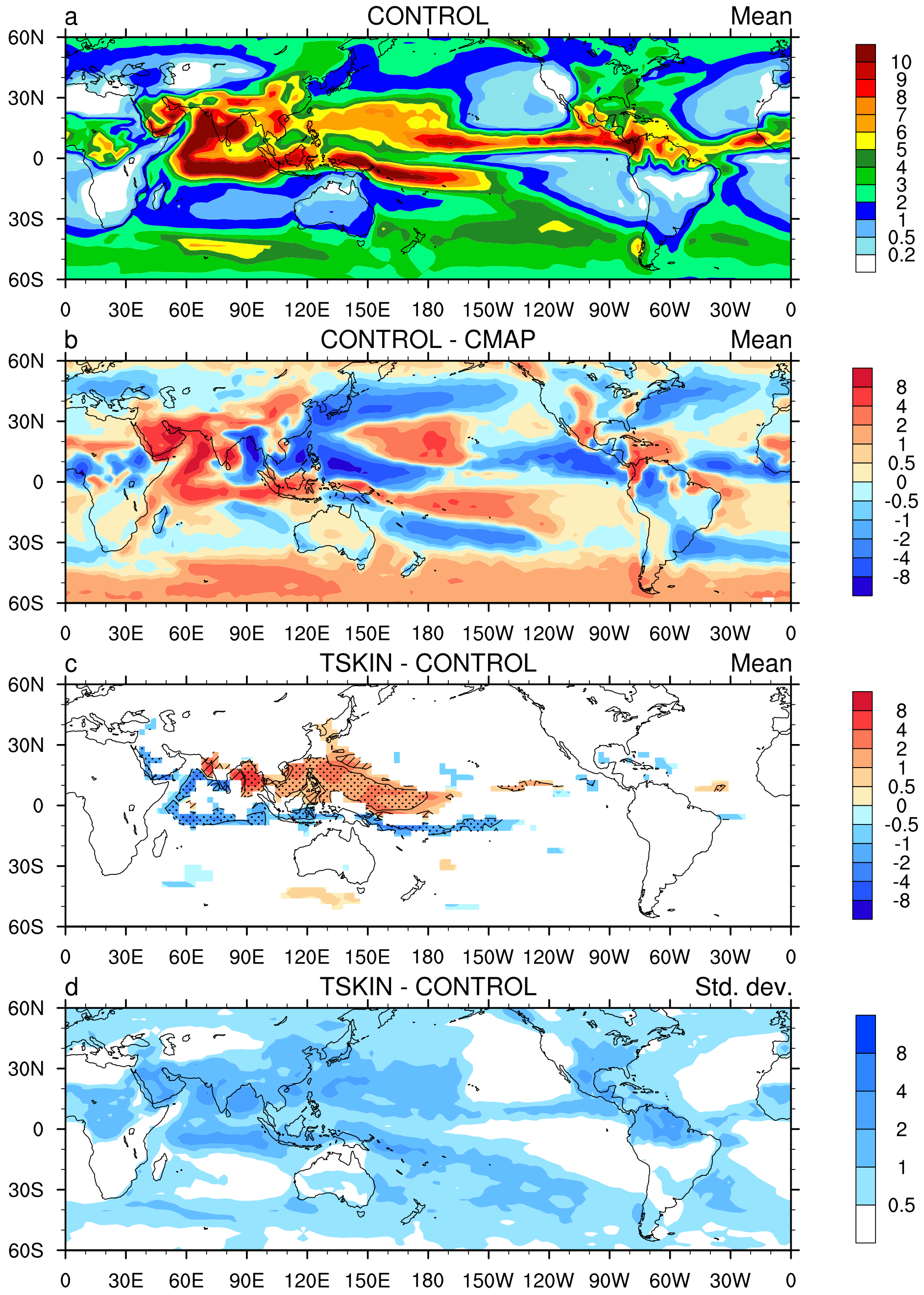

Figure 9. (a) The mean 20-year JJA precipitation rate (mm day^{-1}) in CONTROL, (b) the mean difference between CONTROL and CMAP, (c) the mean difference between TSKIN and CONTROL for areas where this difference is 90% significant with areas where the model is improved relative to CMAP ($|\mathrm{TSKIN} - \mathrm{CMAP}| - |\mathrm{CONTROL} - \mathrm{CMAP}| < -1$ mm day^{-1}, stippled) and worsened ($|\mathrm{TSKIN} - \mathrm{CMAP}| - |\mathrm{CONTROL} - \mathrm{CMAP}| > 1$ mm day^{-1}, slanted lines) further indicated, and (d) the standard deviation of the difference between TSKIN and CONTROL.

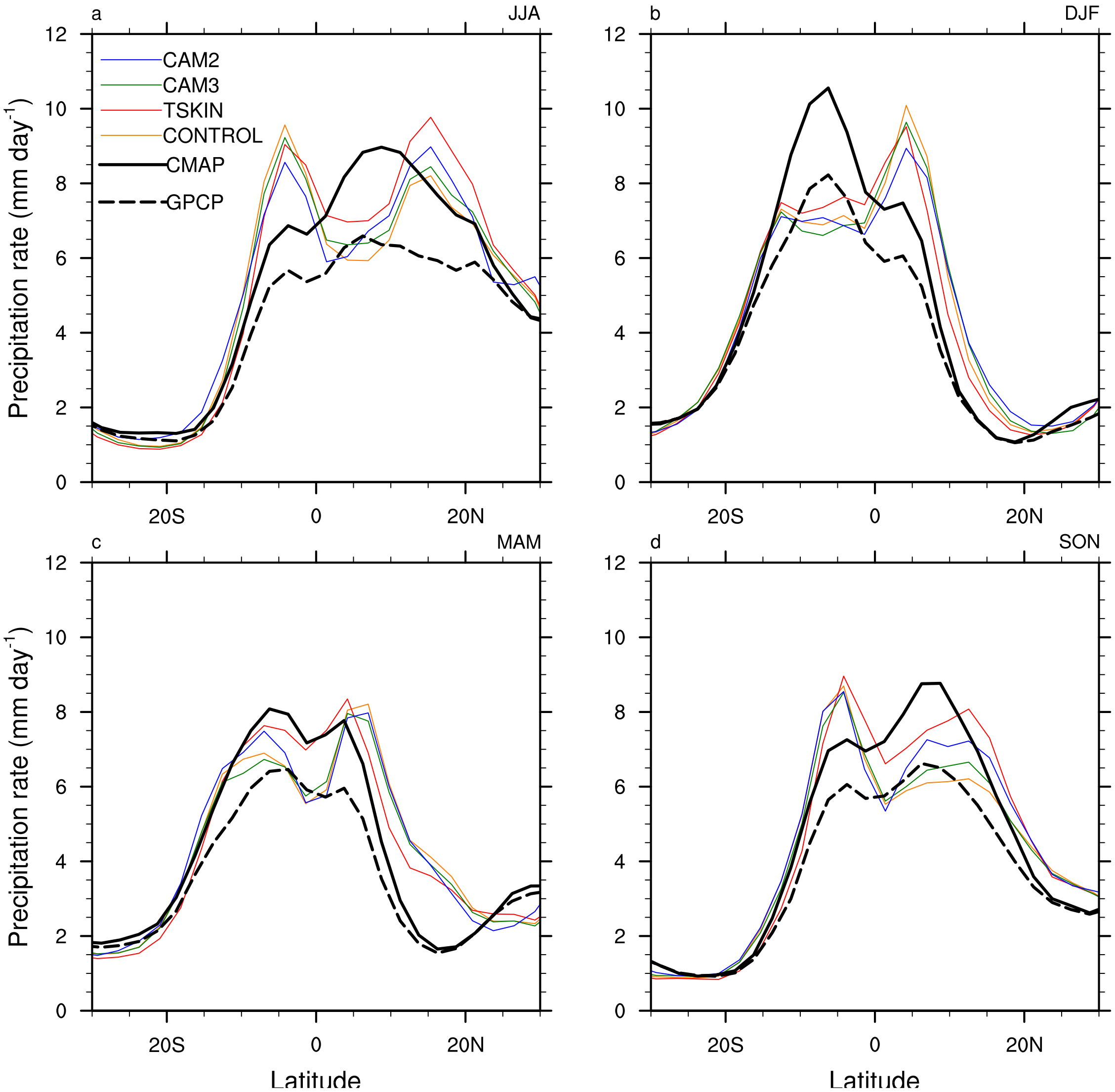

Figure 10. The 20-year zonal mean seasonal precipitation rate between the longitudes of 60°E and 180°E in CONTROL, TSKIN, CMAP, and GPCP as well as from CAM3 and CAM2 using observed SSTs in (a) June–August (JJA), (b) December–February (DJF), (c) March–May (MAM), and (d) September–November (SON).

Arabian Sea however are not, as these winds were too high to begin with in CONTROL (Figure 11b).

4.3. Tropical Intraseasonal Oscillations

[31] *Collins et al.* [2006a] found that CAM3 does not produce realistic tropical intraseasonal, or Madden-Julian, oscillations. This can be seen by comparing the OLR symmetric and antisymmetric significant spectra defined according to *Wheeler and Kiladis* [1999] from AVHRR in Figures 12a and 12b with those from CONTROL in Figures 12c and 12d. *Wheeler and Kiladis* [1999] defined the MJO as eastward-propagating modes (positive wavenumber) having periods between 30 and 96 days, or with frequencies between about 0.03 and 0.01 in Figure 12, appearing in both the symmetric and antisymmetric spectra. Figures 12c and 12d show that the model produces too weak a spectral power at these frequencies and spreads it across eastward- and westward-propagating wavenumbers making them appear to be standing rather than propagating waves. Figures 12e and 12f show that the MJO spectral power is not improved by the addition of ZB in TSKIN and may, in fact, be slightly weakened.

5. Discussion and Conclusions

[32] The implementation of the *Zeng and Beljaars* [2005] (ZB) prognostic skin SST scheme in CAM3.1 has allowed the model to simulate a realistic diurnal cycle in skin SST when using its climatological SST data set. The diurnal range in SST is significantly increased in the tropics and in the summer hemisphere and can be >2 K in isolated areas (e.g., the western Pacific warm pool in JJA, Figure 1b). Similar but smaller diurnal ranges are obtained in a four-member ensemble of the ECMWF NWP model (Figure 13a).

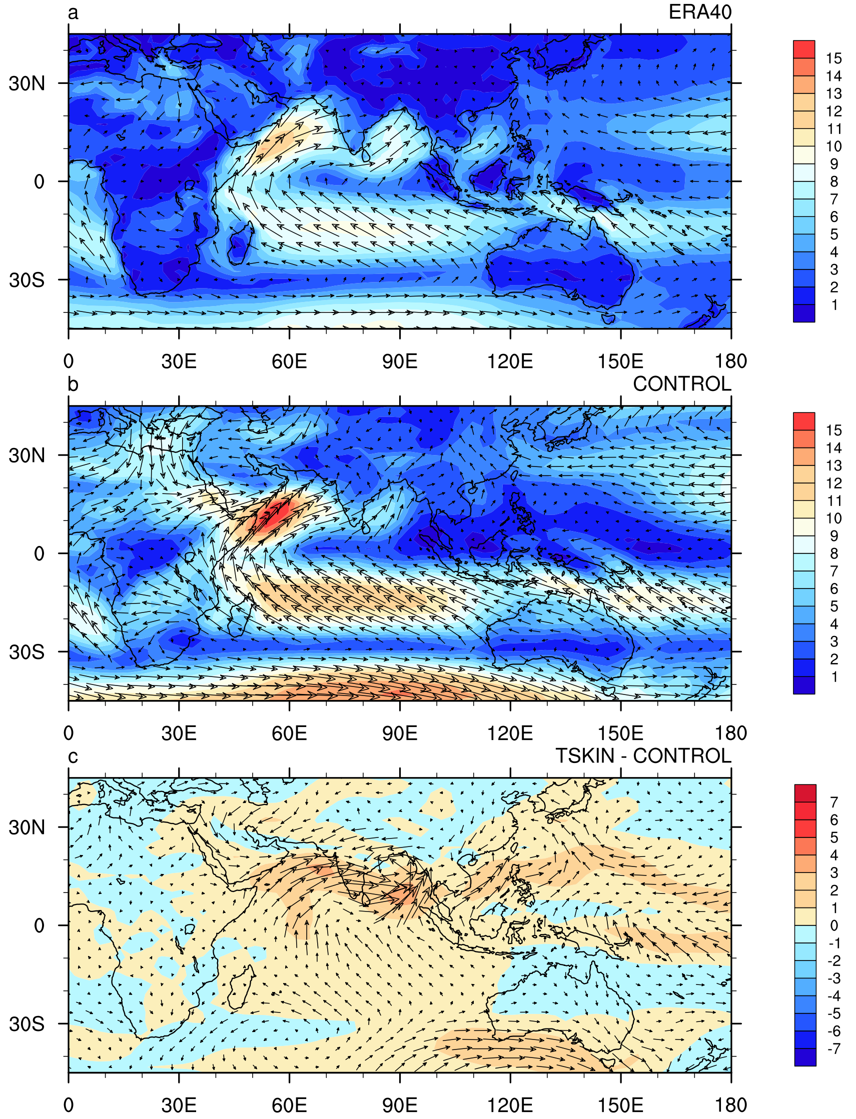

Figure 11. (a) The mean 10-m wind speed (m s^{-1}) from the ERA-40 reanalysis, (b) the mean near-surface wind speed (m s^{-1}) in CONTROL, and (c) the mean difference in near-surface wind speed between TSKIN and CONTROL.

Smaller still are the SST diurnal ranges when the same scheme is implemented in an AGCM coupled to an OGCM [*Misra et al.*, 2008] in which the SST diurnal range is less than 0.2 K in the tropical Pacific (not shown). The lower diurnal ranges in these models are primarily caused by the higher tropical wind speeds than in CAM3.1 (e.g., Figure 13b in ECMWF compared to Figure 1d).

[33] The increased SST diurnal cycle affects the diurnal cycles of other surface quantities such as 2-m air temperature (Figure 2b), latent and sensible heat fluxes (Figure 2d), and precipitation rate (Figure 3b) in CAM3.1. While the maximum amount of precipitation changes in the tropics, the timing of that maximum generally does not change when compared to observations made by the Tropical Atmosphere-Ocean (TAO) buoy array across the Pacific Ocean (Figure 5), but there are other regions in the tropics where there are noticeable changes in this timing in the model (Figure 4).

[34] The effect of the SST diurnal cycle on the seasonal means in CAM3.1 is to at least partially negate some of the biases seen in CONTROL for latent heat flux in the tropics and subtropics (Figure 8) and for total precipitation amount in the tropics (Figure 9c) in some regions. Particularly, the large underestimates in JJA precipitation over the northwest tropical Pacific and the Bay of Bengal as well as the overestimates just south of the equator from the central Pacific into the Indian Ocean and over the Arabian Sea and Peninsula are partially rectified (Figure 9c). Similar results are also obtained by ECMWF. Figure 13c shows the ensemble-mean total precipitation rate difference between versions of ECMWF with and without ZB in the JJA season of 2001. ECMWF is producing similar changes in convective precipitation to

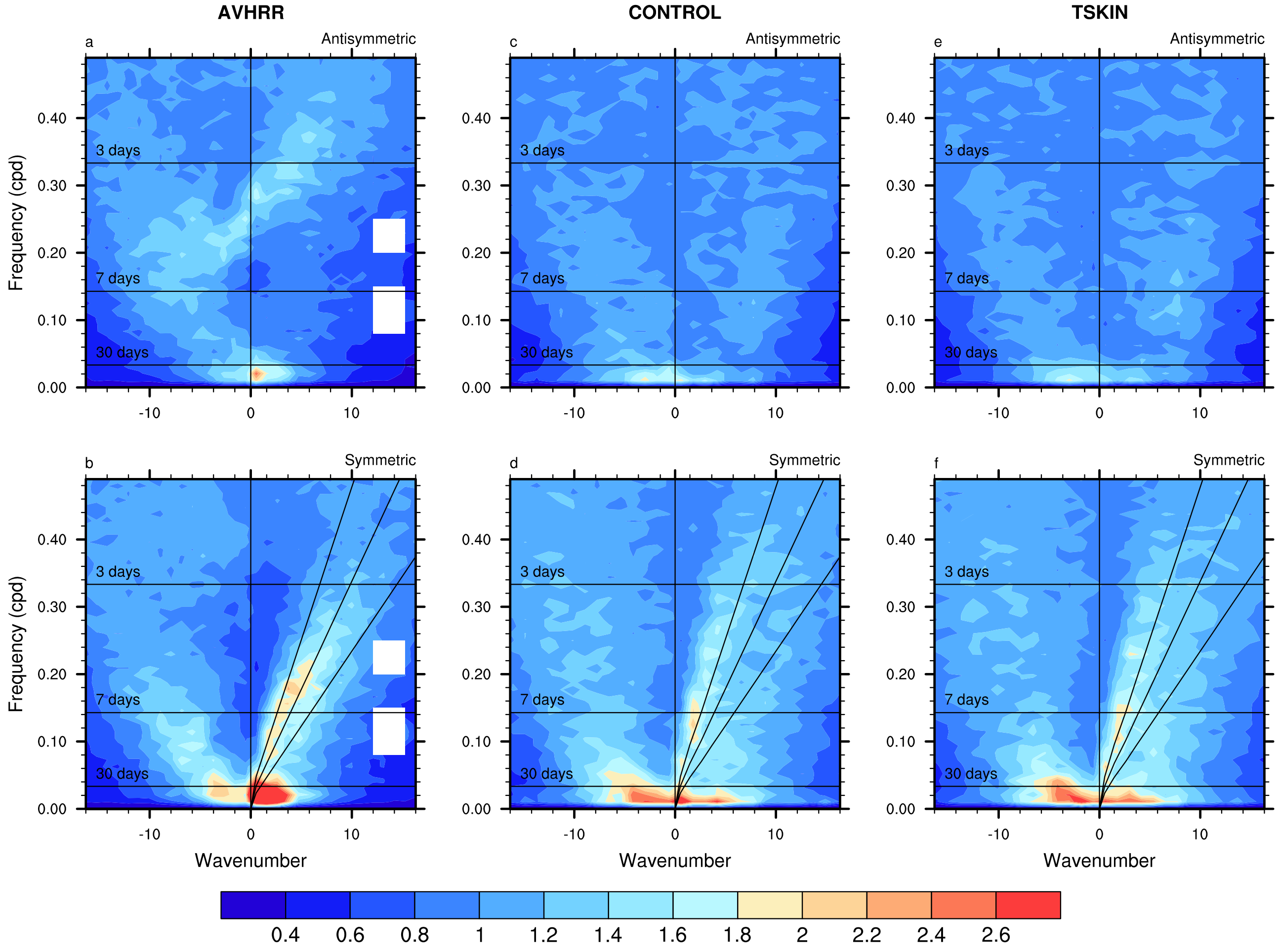

Figure 12. The significant spectral power as a function of wavenumber and frequency (cycles per day) for the (a) antisymmetric and (b) symmetric components from the AVHRR OLR [*Wheeler and Kiladis*, 1999]. Also shown are the spectra from the corresponding components in (c, d) CONTROL and (e, f) TSKIN. Also given are the dispersion curves for Kelvin waves at equivalent depths of (from right to left) 12, 25, and 50 m in Figures 12b, 12d, and 12f.

CAM3.1 although relatively more spatially incoherent. In particular, ECMWF is increasing the convective precipitation over the northwest Pacific, the Northern Hemisphere ITCZ over the central Pacific, and over the Bay of Bengal.

[35] With these tropical precipitation changes, there is a small increase in precipitation in the Northern Hemisphere ITCZ coupled with a small decrease in the Southern Hemisphere ITCZ in JJA in TSKIN (Figure 10a), but TSKIN does not improve the major deficiency in the model of producing a double ITCZ. Figure 13d shows that similar results are also obtained in ECMWF with the inclusion of ZB except that the control simulation is much more realistic without a double ITCZ. In CAM3.1, somewhat similar results to JJA are obtained in DJF (Figure 10b), while in the transitional seasons (MAM, Figure 10c, and SON, Figure 10d), there are large increases in the precipitation in the ITCZ of the fall hemisphere by TSKIN which fall between the rates in CMAP and GPCP.

[36] These changes in CAM3.1 and ECMWF are similar to what was found in ECMWF because of an improvement to the surface turbulent flux parameterization by *Miller et al.* [1992]. As in *Miller et al.* [1992], the improved latent heat fluxes appear to be changing the large-scale flow over the Indian Ocean area. The cross-equatorial and cross-subcontinental flow is increased in TSKIN (Figure 11c) leading to an increase in precipitation along the west coast of India and over the Bay of Bengal (Figure 9c). This represents a slightly more realistic precipitation pattern for the summer monsoon in CAM3.1.

[37] Even though the differences between TSKIN and CONTROL represent a small correction of the biases in CONTROL in some regions, the interannual variability in the model differences can also be on the order of or larger than the model differences (e.g., Figure 9d). Thus TSKIN might produce a larger or smaller difference from CONTROL in a particular region depending on the year. Even so, the realistic diurnal cycle produced in TSKIN does generally produce a relatively larger rectification of biases in the tropics, particularly in tropical precipitation, that is relatively higher than that produced from a random perturbation in the bulk SST (RANDOM). Further model refinement needs to

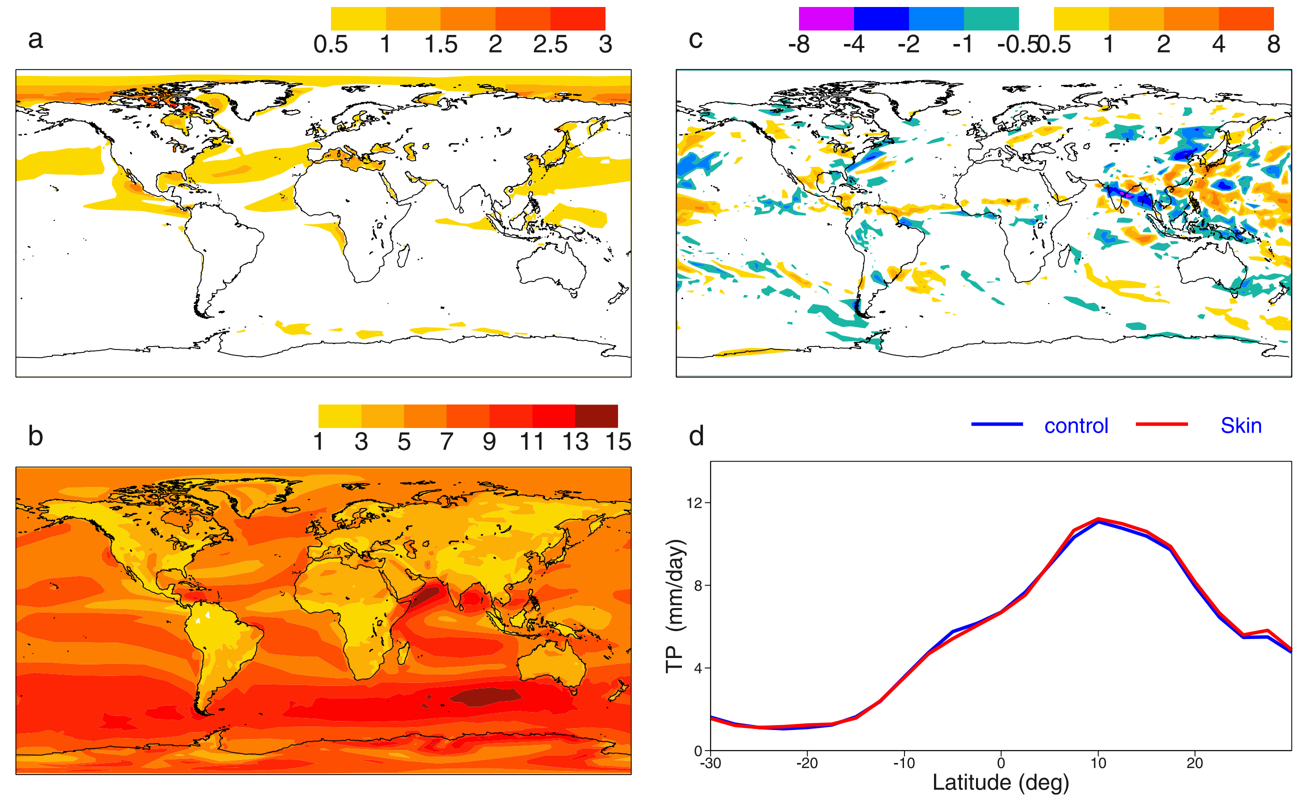

Figure 13. The four ensemble-mean (a) diurnal range in sea surface temperature (SST) and (b) wind speed in an experimental version of the ECMWF model that includes ZB for one JJA season in 2001. (c) The mean difference in total precipitation rate for JJA 2001 between the version of ECMWF with ZB and a control. (d) The zonal mean total precipitation rate in JJA 2001 between 60°E and 180°E in the control version and the version with ZB (Skin).

be made in other ways like changing the convective parameterization, for instance.

[38] Perhaps such changes may help in the simulation of the Madden-Julian oscillation (MJO). Here, the addition of the diurnal cycle in skin SST introduced by ZB had little effect on the MJO produced by CAM3.1. Rather than being eastward-propagating (positive wavenumber), they appear to remain as standing waves and actually may be slightly weaker in strength (Figures 12e and 12f). Several recent studies [*Waliser et al.*, 1999; *Kemball-Cook et al.*, 2002; *Bernie et al.*, 2005; *Woolnough et al.*, 2007] have shown that the simulated MJO was improved upon coupling to either a mixed layer model or fully coupled to an OGCM, so it is possible that a better MJO may be produced with the diurnal variation of the skin SST if CAM3.1 is coupled to the slab ocean model or fully coupled as in the CCSM.

[39] Finally, the ZB algorithm is a cost-effective method to reproduce the diurnal cycle of skin SST without the need to couple to a bulk SST less than once a day. TSKIN runs only 19 seconds more than CONTROL for one year of simulation on a SGI Altix 4700 using 32 nodes. While here ZB added the warm layer and cool skin effects to a climatological SST data set, it could be used on an observed SST data set or coupled to a slab ocean model or a full ocean GCM, which provides the scheme with bulk SST on a daily basis.

[40] **Acknowledgments.** This work was supported by the NSF (ATM360030). We thank ECMWF, the Physical Science Division of NOAA/ESRL, the TAO Project Office at NOAA/PMEL, and NASA for providing their data used in this project. The authors also thank the reviewers for their helpful comments.

References

Adler, R. F., J. Susskind, G. J. Huffman, D. Bolvin, and E. Nelkin (2003), The version 2 Global Precipitation Climatology Project (GPCP) monthly precipitation analysis (1979–present), *J. Hydrometeorol.*, *4*, 1147–1167.

Arkin, P. A., and P. E. Ardanuy (1989), Estimating climatic-scale precipitation from space: A review, *J. Clim.*, *2*, 1229–1238.

Beljaars, A. C. M. (1997), Air-sea interaction in the ECMWF model, paper presented at the Seminar on Atmosphere-Surface Interactions, European Centre for Medium-Range Weather Forecasts, Reading, U.K., 8–12 Sept.

Bernie, D. J., S. J. Woolnough, J. M. Slingo, and E. Guilyardi (2005), Modeling diurnal and intraseasonal variability of the ocean mixed layer, *J. Clim.*, *18*, 1190–1202.

Clayson, C. A., and J. A. Curry (1996), Determination of surface turbulent fluxes for the Tropical Ocean-Global Atmosphere Coupled Ocean-Atmosphere Response Experiment: Comparison of satellite retrievals and in situ measurements, *J. Geophys. Res.*, *101*, 28,515–28,528.

Collins, W. D., et al. (2004), Description of the NCAR Community Atmosphere Model (CAM3), in *Tech. Rep. NCAR/TN-464+STR*, 226 pp., National Center for Atmospheric Research, Boulder, Colo.

Collins, W. D., et al. (2006a), The formulation and atmospheric simulation of the Community Atmosphere Model version 3 (CAM3), *J. Clim.*, *19*, 2144–2161.

Collins, W. D., et al. (2006b), The Community Climate System Model version 3 (CCSM3), *J. Clim.*, *19*, 2122–2143.

Dai, A., and K. E. Trenberth (2004), The diurnal cycle and its depiction in the Community Climate System Model, *J. Clim.*, *17*, 930–951.

Fairall, C. W., E. F. Bradley, J. S. Godfrey, G. A. Wick, J. B. Edson, and G. S. Young (1996), Cool-skin and warm-layer effects on sea surface temperature, *J. Geophys. Res.*, *101*, 1295–1308.

Gentemann, C. L., C. J. Donlon, A. Stuart-Menteth, and F. J. Wentz (2003), Diurnal signals in satellite sea surface temperature measurements, *Geophys. Res. Lett.*, *30*(3), 1140, doi:10.1029/2002GL016291.

Gruber, A., and A. F. Krueger (1984), The status of the NOAA outgoing longwave radiation data set, *Bull. Am. Meteorol. Soc.*, *65*, 958–962.

Kemball-Cook, S., B. Wang, and X. Fu (2002), Simulation of the intraseasonal oscillation in the ECHAM-4 model: The impact of coupling with an ocean model, *J. Atmos. Sci.*, *59*, 1433–1453.

Liebmann, B., and C. A. Smith (1996), Description of a complete (interpolated) outgoing longwave radiation data set, *Bull. Am. Meteorol. Soc.*, *77*, 1275–1277.

McPhaden, M. J., et al. (1998), The Tropical Ocean-Global Atmosphere observing system: A decade of progress, *J. Geophys. Res.*, *103*, 14,169–14,240.

Misra, V., L. Marx, M. Brunke, and X. Zeng (2008), The equatorial Pacific cold tongue bias in a coupled climate model, *J. Clim.*, *21*, 5852–5869.

Miller, M. J., A. C. M. Beljaars, and T. N. Palmer (1992), The sensitivity of the ECMWF model to the parameterization of evaporation from the tropical oceans, *J. Clim.*, *5*, 418–434.

Negri, A. J., R. F. Adler, and L. Xu (2002), A TRMM-calibrated infrared rainfall algorithm applied over Brazil, *J. Geophys. Res.*, *107*(D20), 8048, doi:10.1029/2000JD000265.

Rasch, P. J., et al. (2006), A characterization of tropical transient activity in the CAM3 atmospheric hydrologic cycle, *J. Clim.*, *19*, 2222–2242.

Rayner, N. A., D. E. Parker, E. B. Horton, C. K. Folland, L. V. Alexander, D. P. Powell, E. C. Kent, and A. Kaplan (2003), Global analyses of sea surface temperature, sea ice, and night marine air temperature since the late nineteenth century, *J. Geophys. Res.*, *108*(D14), 4407, doi:10.1029/2002JD002670.

Reynolds, R. W., and T. M. Smith (1994), Improved global sea surface temperature analyses using optimum interpolation, *J. Clim.*, *7*, 929–948.

Reynolds, R. W., N. A. Rayner, T. M. Smith, D. C. Stokes, and W. Wang (2002), An improved in situ and satellite SST analysis for climate, *J. Clim.*, *15*, 1609–1625.

Serra, Y. L., and M. J. McPhaden (2003), Multiple time- and space-scale comparisons of ATLAS buoy rain gauge measurements with TRMM satellite precipitation measurements, *J. Appl. Meteorol.*, *42*, 1045–1059.

Serra, Y. L., and M. J. McPhaden (2004), In situ observations of diurnal variability in rainfall over the tropical Pacific and Atlantic Oceans, *J. Clim.*, *17*, 3496–3509.

Serra, Y. L., P. A'Hearn, H. P. Freitag, and M. J. McPhaden (2001), ATLAS self-siphoning rain gauge error estimates, *J. Atmos. Ocean. Technol.*, *18*, 1989–2002.

Uppala, S. M., et al. (2005), The ERA-40 re-analysis, *Q. J. R. Meteorol. Soc.*, *131*, 2961–3012.

Waliser, D. E., K. M. Lau, and J.-H. Kim (1999), The influence of coupled sea surface temperatures on the Madden-Julian oscillation: A model perturbation experiment, *J. Atmos. Sci.*, *56*, 333–358.

Webster, P. J., C. A. Clayson, and J. A. Curry (1996), Clouds, radiation, and the diurnal cycle of sea surface temperature in the tropical western Pacific, *J. Clim.*, *9*, 1712–1730.

Wheeler, M., and G. N. Kiladis (1999), Convectively coupled equatorial waves: Analysis of clouds and temperature in the wavenumber-frequency domain, *J. Atmos. Sci.*, *56*, 374–399.

Woolnough, S. J., F. Vitart, and M. A. Balmaseda (2007), The role of the ocean in the Madden-Julian oscillation: Implications for MJO prediction, *Q. J. R. Meteorol. Soc.*, *133*, 117–128.

Xie, P., and P. A. Arkin (1997), Global precipitation: A 17-year monthly analysis based on gauge observations, satellite estimates, and numerical model outputs, *Bull. Am. Meteorol. Soc.*, *78*, 2539–2558.

Zeng, X., and A. Beljaars (2005), A prognostic scheme of sea surface skin temperature for modeling and data assimilation, *Geophys. Res. Lett.*, *32*, L14605, doi:10.1029/2005GL023030.

Zeng, X., M. Zhao, R. E. Dickinson, and Y. He (1999), A multiyear hourly sea surface skin temperature data set derived from the TOGA TAO bulk temperature and wind speed over the tropical Pacific, *J. Geophys. Res.*, *104*, 1525–1536.

A. Beljaars, European Centre for Medium-Range Weather Forecasts, Reading RG2 9AX, UK. (anton.beljaars@ecmwf.int)

M. A. Brunke and X. Zeng, Institute of Atmospheric Physics, University of Arizona, Physics-Atmospheric Sciences Building, P.O. Box 210081, Tucson, AZ 85721-0081, USA. (brunke@atmo.arizona.edu; xubin@atmo.arizona.edu)

V. Misra, Department of Meteorology, Florida State University, Room 404 Love Building, 1017 Academic Way, P.O. Box 3064520, Tallahassee, FL 32306-4520, USA. (vmisra@met.fsu.edu)